Lawrence Berkeley Laboratory
UNIVERSITY OF CALIFORNIA

Materials & Chemical Sciences Division
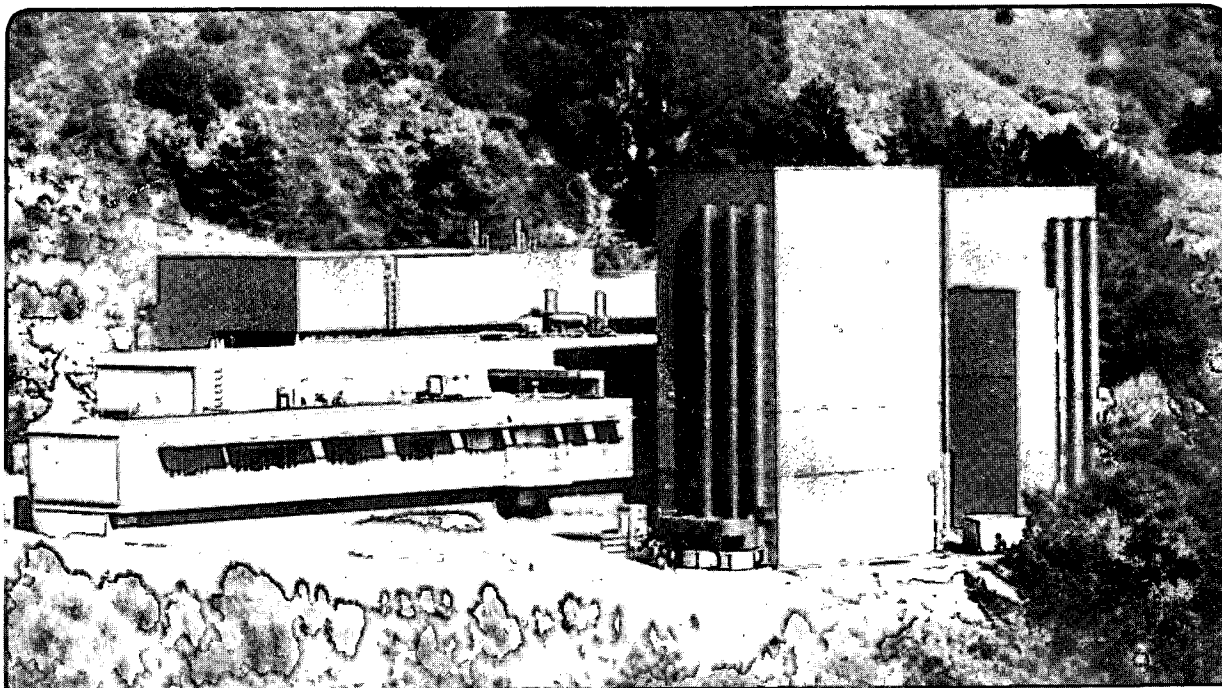
National Center for Electron Microscopy

Atomic Imaging of 3:2 Mullite

T. Epicier, M.A. O'Keefe, and G. Thomas

July 1989

DISCLAIMER

ATOMIC IMAGING OF 3:2 MULLITE

T. Epicier[*] , M.A. O'Keefe and G. Thomas

National Center for Electron Microscopy, Materials and Chemical Science Division, Lawrence Berkeley Laboratory, 1 Cyclotron Road, Berkeley, California 94720 USA

Abstract: the crystallographic structure of $3Al_2O_3-2SiO_2$ mullite has been studied by means of High Resolution Electron Microscopy. The best conditions for atomic imaging of this compound are discussed relative to the Atomic Resolution Microscope at Berkeley. [001] multibeam images have been produced at 0.19nm resolution, allowing the cation sublattice to be directly imaged, with a firm transfer of information on the oxygen sublattice. Under optimal conditions of defocus setting and thickness, typical contrasts have been detected and consistently interpreted in terms of the presence of oxygen vacancies along the defective atomic columns. These observations are discussed in relation to the currently accepted model for the average structure of mullite.

Introduction

Mullite is an aluminium-silicate mineral whose composition ranges from approximately $3Al_2O_3-2SiO_2$ to $2Al_2O_3-1SiO_2$. The ratio "Al_2O_3/SiO_2" (designated hereafter as [M:N]) may be used to characterize the chemical composition of mullite whose complete formula then appears to be $Al_{4+2x}Si_{2-2x}O_{10-x}$, where x designates the number of oxygen atoms missing per average unit cell; relations between x and [M:N] are:

$$x = 2\frac{[M:N]-1}{2[M:N]+1} \text{ and } [M:N] = \frac{1+x/2}{1-x} \quad (1)$$

[*]permanent address : INSA, GEMPPM, Bât. 502, u. a. CNRS 341, 69621 Villeurbanne Cedex, France.

Most interest concerning mullite arises from the fact this compound is a potential candidate for high temperature applications in the ceramic materials field. Moreover, the exact crystallography of mullites, depending upon the M:N ratio, is still the subject of refinement. Both aspects have led us to undertake a structural characterization of various 3:2 mullites by means of High Resolution Electron Microscopy (HREM). It will be shown in this paper that mullite can be atomically imaged at a resolution better than 0.2nm[1], using the Atomic Resolution Microscope (ARM) at the NCEM; this has made it possible to examine at a very local scale the atomic reorganization occuring around oxygen vacancies, which appear to be randomly distributed in the studied compounds.

Crystallographic Background

The structure of mullite has been studied by many authors and is well documented throughout the literature (Angel, 1986; Burnham, 1964; Cameron, 1977; Saalfield, 1981; Sadanaga, 1962; Tokonami et al., 1980). It consists of octahedral AlO_6 chains parallel to the c-axis and cross linked by tetrahedral $(Al, Si)O_4$ chains (see table 1 and figure 1 for details).

Due to the presence of some oxygen vacancies on O_3 sites (figure 1c), one has to deal with the average cell shown in figure 1a, rather than the perfect cell depicted in figure 1b. For Al-rich mullite (x ≥ 0.40, i.e. compositions near M:N = 2:1), both X-ray (Angel & Prewitt, 1987; Saalfield, 1979; Tokonami et al., 1980) and electron (Cameron, 1977; Kriven & Pask, 1983; Nakajima & Ribbe, 1981; Smith & McConnell, 1966) single crystal diffraction patterns exhibit diffuse or sharp superstructure reflections which indicate a tendency for the ordering of the vacancies. These superstructures have recently been explained in terms of a symmetry analysis for incommensurate modulated structures (McConnell & Heine, 1985). HREM has been used to reveal directly the ordered microstructure of such compounds: "superstructure images" have been produced by just including superlattice beams in the objective aperture, and sets of white dots, associated with the presence of vacancy columns, have been imaged in the [010] orientation (Nakajima et al.,

1975; Yla-Jaaski & Nissen, 1983)[a]. Such observations do not, however, allow the atomic displacements around individual vacancies (see figure 1c) to be resolved because of insufficient resolution under the conditions used by these authors. "Structure imaging" has recently been attempted (Schryvers et al. 1988) in the [001] orientation on a $1.7Al_2O_3$-$1SiO_2$ mullite; although reliable, their observations do not allow the structure to be imaged at an acceptable resolution in order to discuss the previous point. The present work was then undertaken to examine the conditions under which the structure of mullite can be correctly imaged in HREM, and consequently, to check the atomic displacements previously refined by macroscopic diffraction techniques.

Experimental

1. specimen

Two types of polycrystalline 3:2 mullites have been used in the present investigation. The first one (labelled K hereafter) is from the Kyocera company, and the second one (T) has been sintered from the Baikowski 193 CR starting powder (Torrecillas, 1987). The composition has been ascertained in both cases by chemical analysis in the microscope as described in sub-section 2.

Thin foils adequate for the Transmission Electron Microscopy work have been conventionally prepared by ion-beam thinning (5.5 kV argon beams, incidence angle 30°); a carbon coating was performed in order to avoid charging under the electron beam.

2. chemical analysis

The chemical analysis of the samples was achieved on a JEOL 200 CX microscope, equipped with an ultra-thin window detector and a Kevex 8000

---

[a] Details about the so-called "superstructure imaging" in HREM may be found (Hiraga et al. 1981); a specific study concerning imaging of ordered carbon vacancies in a sub-stoichiometric carbide, which may serve as a generic example for imaging the ordered distribution of vacancies on a light element sublattice, has also recently been reported (Epicier et al. 1989).

Analyst. Data obtained by a simultaneous analysis of oxygen, aluminium and silicon in several grains have been consistently interpreted and final results are:

.K sample: Al_2O_3: 73.33±0.5 wt%; SiO_2: 26.66±0.5 wt%, i.e. [M:N] = 3.30/2.00 (x ≈ 0.30)
.T sample: Al_2O_3: 71.46±0.5 wt%; SiO_2: 28.54±0.5 wt%, i.e. [M:N] = 3.00/2.00 (x = 0.25).

Impurities were not detected in the mullite grains of any of these compounds.

3. HREM observations

The High Resolution study was conducted on the Atomic Resolution Microscope at the NCEM. The operating conditions, as well as the required data for computer multislice simulations using both SHRLI (O'Keefe & Buseck, 1979) and CEMPAS (Kilaas, 1987) packages, are summarized in table 2.

The observations were limited to the [001] orientation, since it was checked by preliminary calculations that other low-index azimuths do not allow the structure to be imaged at a sufficient resolution.

Extensive "through-focus series" were recorded in order to ascertain the structure through the examination of several consistent images; the defocus values were deduced from the manufacturer's calibration of the focusing controls and also directly estimated from the analysis of diffractograms from amorphous regions on an optical bench. Occasional digitizing of the micrographs at a resolution of 2048 by 2048 pixels with an Eikonix 78/99 camera controlled by a locally-written command incorporated into the SEMPER programs of Saxton et al., (1979) was performed for numerical treatment and improvement of the experimental images by spatial filtering.

Results

1. required resolution for "structure imaging" of mullite

In order to know the range of information available at a given experimental resolution, a set of calculations of "Weak-Phase Object" (WPO) images was carried out . Figure 2 shows these images as projections of the crystal-structure potential to the resolutions indicated. From these theoretical images, it clearly appears that (provided one obtains a suitably thin specimen), an experimental resolution of at least 0.19nm to 0.17nm is needed if one wants to detect the presence of oxygen around cations, while attempting to image simultaneously the cation sublattice. Also, it is seen that a resolution of 0.24nm, which roughly corresponds that available on current 100 or 200 kV microscopes (as those used in earlier high resolution microscopy investigations on mullite (Nakajima et al., 1975; Ylar-Jaaski & Nissen, 1983; Eberhard et al., 1986)), is insufficient to achieve this goal. Ideally, a 0.12nm resolution, which has not yet been experimentally obtained on any existing microscope, would be required for separating both cation and anion atomic columns (figure 2).

2. best experimental conditions for atomic imaging of mullite

From the above, the demonstrated resolution of the ARM (< 0.17nm, as indicated in table 2) is adequate for transferring actual image information on the oxygen atoms (and vacancies) in the case of mullite. However, the peculiarities of the Contrast Transfer Function (CTF) of the ARM make it worth examining in detail the setting of the focussing conditions for optimal imaging of the structure of mullite. Figure 3 reproduces two CTF plots for two defocus values of particular interest, Δf_1 and Δf_2, respectively equal to - 55nm and -80nm (where underfocus is assigned negative values) and roughly corresponding to n = 1 and 2 in the following formula:

$$\Delta f_n = -\sqrt{(1+n/2)\, C_s\, \lambda} \qquad (2)$$

(λ is the electron wavelength, viz. 0.00102nm at 800 kV).

Due to the particular shape of the damping envelope caused by chromatic aberration, it is seen in figure 3 that the setting of the defocus to Δf_2 provides a better transfer of spatial frequencies associated with distances in the 0.2-0.17nm range than that corresponding to Δf_1 (Scherzer defocus). Moreover,

the CTF zero near $(0.25nm)^{-1}$ will probably lead to an improvement of the signal-to-noise ratio, since undesirable information due to contamination is generally expected to be transferred in the 0.20nm - 0.25nm range. Then, Δf_2 should be preferred for imaging details below 0.2nm. Unfortunately, it is seen that the setting at Δf_2 gives rise to a sign inversion for frequencies associated with distances respectively higher and lower than $d_0 \approx 0.26nm$: in the classical WPO approximation (Spence, 1980), this would lead to dark contrast for atomic columns at the intersection of lattice fringes of inter-reticular distances higher than d_0, and white contrast otherwise. When dealing with mullite, it appears that this situation will not allow better images to be obtained by using Δf_2, although this setting permits a better transfer of the highest spatial frequencies. This is clearly demonstrated in figures 4 and 5. As will be seen below, it also appears that Δf_1 is the best defocus value for obtaining multibeam images with the finest scale of details.

Further questions may be posed about the influence of lens focus setting on the quality of high resolution micrographs of mullite. Figure 6a shows a set of calculated images at different defocus values for a reasonably low thickness (these images are calculated from the structural model of figure 1a).

The "best" type of images are only obtained near the Scherzer defocus as experimentally observed (see figure 4). The experimental micrographs of figure 6b are from wide through-focus series which are self-consistent and exhibit excellent agreement with the simulated images of figure 6a. As already mentioned, the resolution remains rather poor for most defocus values, except near the Scherzer defocus.

Examination of wedge-shaped crystals reveals how the thickness influences the contrast of experimental images. From figure 7, it is seen that the "structure image" aspect of the micrographs is already severely perturbed for thicknesses as low as $t_2 = 8nm$. For thicker crystals, the Scherzer defocus condition no longer enables the atomic structure of mullite to be directly imaged; moreover, it appears that even a little crystal tilt (unavoidable in practice, even through a careful alignment of the zone axis in the Selected Area Diffraction Mode) has a drastic influence on the experimental contrast -

see figure 7c and comments in caption.   This point was previously investigated (Schryvers et al., 1988).   However, the present analysis of thickness and tilt effects explains why their ARM micrographs, frequently obtained at thicknesses as large as 8nm, and at defoci different than the Scherzer value, did not allow the structure of mullite to be clearly resolved.

From the above, it can be pointed out that atomic imaging of mullite can be successful only on very thin crystals (less than 6nm nominally) at the Scherzer defocus condition.

3. Artefacts due to microscope misalignment

Among the various adjustments that have to be done for atomic-resolution imaging, the beam alignment in the objective lens and the correction of objective lens astigmatism are of critical importance (Smith et al., 1983).

The special tilt alignment device available on-line on the ARM (Hetherington et al., 1989) enables the operator to set the beam parallel to the optic axis with an accuracy of about 0.5 mrad. This angle is less than the semi-angle of beam convergence, $\theta_c = 0.8$ mrad. An academic investigation of beam misalignment effects reveals that a tilt as large as ≈ 2.5 mrad must be considered in order to see a significant change in the experimental contrast (see figure 8).   Such misorientations are much greater than the accuracy mentioned above, and this effect can be ignored if the alignment procedure is normally followed.

Astigmatism corrections were performed through the usual method based on the refinement of the "zero contrast" focusing of the amorphous edge. However, a major problem appeared when this contamination layer was insufficient (see figure 9a), since astigmatism correction directly on the aspect of the crystal image appeared to be extremely delicate, due to the lack of simple symmetries in the correctly adjusted Scherzer image (see figure 4). It appeared that a good adjustment was possible by underfocussing the image in order to obtain the almost perfect four-fold symmetric images shown in figure 6 for defoci ranging between -80nm and -130nm nominally. It must be noticed that even low astigmatism produced a tremendous change

in image contrast (see figure 9b), making any interpretation meaningless, and even inviting dangerous false conclusions, since the predominant white dots in figure 9b - due to astigmatism - might, according to the literature (Yla-Jaaski & Nissen, 1983; Epicier et al., 1989), suggest the presence of ordered vacancy columns.

4. detection of oxygen vacancies

The micrographs reported in figure 10 show a reliable analysis of the structure of the 3:2 mullite in the case of the sample K (see caption for detailed comments).
As can be seen from the regions arrowed in figure 10a, typical defect contrasts have been detected, which will be shown to be consistent with the presence of oxygen vacancies within the crystal. From the extensive calculations reported in the appendix, and summarized in figure 10e, a good description of these defects has been realized assuming the existence of half vacant oxygen columns in the foil. Considering the low thickness of the examined area, this corresponds to the presence of 2 to 4 vacancies along the defective atomic rows. The apparently random distribution of such defects strongly supports the commonly accepted hypothesis that oxygen vacancies are disordered in the 3:2 compound. Furthermore, conventional electron diffraction analysis of the samples gave no evidence for superlattice reflections.

Moreover, it can be said that there is no hope of resolving the presence of any single point defect, since according to the simulated images reported in the appendix, vacancy occupancies lower than about 0.5 do not give rise to any detectable contrast. It is also clear that the average structure of figure 1a correctly describes the crystal in most areas, except in those where the random distribution of vacancies is such that the occupancy of displaced T*-type columns becomes higher than 0.5 (see appendix).

Thus it is concluded that the good agreement between the experimental contrast of the defects, and that calculated from the configuration shown in figure 1c (assuming the atomic displacements corresponding to the positions

given in table 1) provides further confirmation of the atomic model around vacancies previously deduced from x-ray analysis of various mullites.

Conclusion

The present work was undertaken in order to determine the limits of the HREM technique in the study of the structure of mullite. Mullite 3:2 compounds were examined with the ARM, and the results can be summarized as follows:

1) The atomic imaging of mullite is successful, due to the excellent point resolution of the microscope, viz. below 0.2nm.

2) Very precise requirements concerning the imaging conditions (defocus value, thickness, beam tilt and astigmatism correction) must be fullfilled in order to allow interpretable imaging of this compound to be made.

3) In extremely thin areas, defects have been observed and consistently discussed in terms of the presence of oxygen vacancies along the O_3-type columns; the detection of these defects is possible, due to the occurrence of at least 50% of cation displacements from nearest-neighbor T to T^*-type columns.

4) From our observations, it is clear that oxygen vacancies are randomly distributed in the 3:2 compounds studied here.

Acknowledgements

References

(1)   R.J. Angel, C.T. Prewitt, Am. Mineral. **71** (1986), p. 1476

(2)   R.J. Angel, C.T. Prewitt, Acta Cryst. B**43** (1987), p. 116

(3)   C. Burnham, Carnegie Inst. Wash. Year Book **62** (1963), p. 158, and *ibid*, **63** (1964), p. 223

(4)   W. E. Cameron, Am. Mineral. **62** (1977), p. 747

(5)   E. Eberhard, S. Hamid Rahman, H.T. Weichert, Zeit. Kristallogr. **174** (1986), 1-4, p. 44

(6)   T. Epicier, G. Fuchs, P. Ferret, M.G. Blanchin, Philos. Mag. A **59** (1989), 4, p. 885

(7)   C.J.D. Hetherington, E.C. Nelson, K. Westmacott, R. Gronsky, G. Thomas, to appear in Mat. Res. Soc. Symp. Proc. (1989), 139

(8)   K. Hiraga, D. Shindo, M. Hirabayashi, J. Appl. Cryst. **14** (1981), p. 169

(9)   R. Kilaas, Proc. 45th Ann. Meeting EMSA, San Francisco: G.W. Bailey, (1987), p. 66

(10)   W.M. Kriven, J.A. Pask, J. Am. Cer. Soc. **66** (1983), 9, p. 649

(11)   J.D.C. Mc Connell, V. Heine, Phys. Rev. B **31** (1985),9, p. 6140

(12)   Y. Nakajima, N. Morimoto, E. Watanabe, Proc. Japan Acad. **51** (1975), 3, p. 173

(13) Y. Nakajima, P.H. Ribbe, Am. Mineral. **66** 1981), p. 142

(14) M.A. O'Keefe, P.R. Buseck, Trans. Am. Crystallogr. Assoc. **15** (1979) p. 27

(15) H. Saalfeld, W. Guse, N. Jb. Miner. Mh. **4** (1981) p. 145

(16) H. Saalfeld, N. Jb. Miner. Mh. **3** (1979), p. 305

(17) R. Sadanaga, M. Tokonami, Y. Takéuchi, Acta. Cryst. **15** (1962), p. 65

(18) W.O. Saxton, T.J. Pitt, M. Horner, Ultramicrosc. **4** (1979), p. 343

(19) D. Schryvers, K. Srikrishna, M.A. O'Keefe, G. Thomas, J. Mater. Res. **3** (1988), 6, p. 1355

(20) D. G. W. Smith, J.D.C. McConnell, Miner. Mag. **35** (1966), p. 810

(21) D.J. Smith, W.O. Saxton, M.A. O'Keefe, G.J. Wood, W.M. Stobbs, Ultramicrosc. **11** (1983), p. 263

(22) J.C.H. Spence, Experimental High Resolution Electron Microscopy, Oxford: Clarendon Press, (1980)

(23) M. Tokonami, Y. Nakajima, N. Morimoto, Acta Cryst. A**36** (1980), p. 270

(24) R. Torrecillas, (1987), unpublished work

(25) J. Yla-Jaaski, H.U. Nissen, Phys. Chem. Minerals **10** (1983), p. 47

APPENDIX

For interpreting the defect contrast observed on figure 10d, multislice simulations have been carried out for a wide range of vacancy contents along the defect column. Using an option to stack different elementary slices in the multislice calculations, several thin foils consisting of intercalated "perfect" cells (as the one shown in figure 1b) and "imperfect" ones corresponding to the model of figure 1c have been constructed. For computational reasons, we have used a 4 by 4 supercell in each case, which also allows the result to be untroubled by artefacts arising from the borders of the cells (the actual size of the supercell was then 3.02nm by 3.07nm). In so doing, we were actually able to describe physical stacking sequences. Depending of the total number of stacked cells, it was obviously not possible to increase continuously the vacancy content from 0 to 1, but particular values could be obtained while increasing the vacancy number from 0 to the total number of sites available in a column of any given thickness.

Figure A1 is a matrix of calculated images for the three defocus values experimentally obtained (see figure 10d). In order to check the sensitivity of the defect contrast with respect to the thickness, calculations were run for three reasonable thicknesses for which the perfect average cell of figure 1a matches the experimental images very well. These simulations can be analysed using three distinct features which are visible in figure A2, and described below:

    .feature 1: for a high vacancy content, the parallel straight lines defined by the black dots imaging cations around the defect columns become curved and are displaced away from each other in the -50nm image.

    .feature 2: under the same vacancy conditions, but at -87.5nm defocus, the white dots associated by pair and located at the emplacement of the defective O_3-type column in the greatest underfocused images clearly become closer and brighter than in the perfect crystal image.

    .feature 3: in the images at -97.5nm defocus, and for vacancy contents approaching 1, the white dots close to the defect and aligned parallel to the direction of displacement in feature 1 become diffuse and elongated.

These three particular features allow acceptable ranges of vacancy content to be assigned to the experimental images; clearly, concentrations lower than 0.4 nominally (the lower two images in each column of fig.A.1), cannot fit the microgaphs of figure 10d, since they do not lead to a detectable contrast for feature 1. Similarly, feature 3, which is not observed experimentally, allows the highest vacancy contents, above 0.8 nominally, to be eliminated. All things considered, a compromise agreement is obtained for all three features if we assume a vacancy content of around 0.5, whatever the thickness. The case of 0.5 vacancy content for the lowest thickness (i.e. two vacancies along the 4-cells long [001] column), has been reproduced with an adjusted contrast in figure 10e.

Further remarks need to be made to complete this analysis. As deduced from figure A3, it is clear that the defect contrast is mainly due to the displacement of metallic atoms, rather than to the vacancies themselves. From the above, we can conclude that oxygen vacancies can be detected if at least half of the metallic atoms along each of the T-type columns close to a defective O_3-type column have been displaced into T* sites (Figure 1).

An elementary numerical approach allows the probability $p(\tau,t)$ for having at least a fraction τ of metallic atoms displaced (due to the presence of τ vacancies on the O_3 first neighbour site) along a T-type column of thickness t to be calculated under the assumption of a random distribution of the oxygen vacancies (that is, according to the data from tables 1 and 2, an average occupancy factor of $1-x/2$ for the T sites, or 0.85 in the case of the K-mullite).

The results are shown in figure A4. The full line curve corresponds to the general case where no restriction applies to the way vacancies are distributed along the defect column; for a crystal thickness varying from 0.87nm to 2nm, $p(0.5,t)$ decreases from 12% to $\approx$ 1%, indicating a low probability of detecting defective O_3-type columns. However, it is strongly believed that this situation is not realistic: a totally random distribution allows two vacancies to be in first nearest-neighbour positions at z_0 and $z_0 + |c|$ along an O_3-type column. Previous HREM results on ordered mullite near the 2:1 composition suggest that vacancies avoid the nearest-neighbour positions,

since they always appear to be separated by at least a fully occupied O_3 site along the c-axis (Nakajima, et al., 1975; Yla-Jaaski & Nissen, 1983). Adding this constraint to the random distribution leads to the dashed curve in figure A4, which clearly shows that the probability of detecting oxygen vacancies is then considerably lowered, since it now remains below 2% for thicknesses varying from 0.87nm to 1.5nm. It is believed that this situation might describe the experimental observations reported in figure 10 on the K-mullite.

Moreover, and whatever the restrictions applied to the actual distribution of vacancies, it is clear that the probability of detecting defective columns rapidly approaches zero for thicknesses larger than 2.5nm nominally; this explains why no defect contrast is experimentally discerned for thick crystals. Obviously, the probability is expected to be higher for very low thicknesses (17% at 0.56nm , i.e. a two cells thick crystal, as shown in figure A4), but such ideally thin foils are, in pratice, either inobservable or at least not representative of the bulk state, due to contamination or perturbation caused by probable atomic relaxations.

Table 1

space group Pbam
a=0.754nm
b=0.768nm
c=0.2885nm

atom	designation	x	y	z	occupancy	Debye-Waller (nm^2)
Al	Al$_1$ (2a)	0.	0	0	1.	.0045
Al	T (4h)	0.351	0.159	0.5	0.54	.0054
Si	T (4h)	0.351	0.159	0.5	0.33	.0054
Al	T* (4h)	0.236	0.294	0.5	0.1	.005
Si	T* (4h)	0.236	0.294	0.5	0.03	.005
O	O$_1$ (4g)	0.374	0.283	0	1.	.01
O	O$_2$ (4h)	0.139	0.076	0.5	1.	.01
O	O$_3$ (2d)	0.	0.5	0.5	0.63	.01
O	O* (4h)	0.053	0.447	0.5	0.13	.01

Table 1: crystallographic data concerning the 3:2 mullite (x = 0.25) compiled from the literature and used in the present work (the designation of the Wyckoff positions is given between parentheses in the second column, and Debye-Waller factors are given in nm^2). The occupancy factors roughly follow the general relationships over the whole compositional range:

.occ = 1-x/2 for T (Al + Si) sites
.occ = 1-3x/2 for O$_3$ sites
.occ = x/2 for O* and T* (Al + Si) sites.

Table 2

Experimental and computing data for the HREM work.

.accelerating voltage...800kV

.spherical aberration coefficent C_s...2 mm*

.spread of focus...15nm*

.semi-angle of beam convergence..0.8 mrad**

.objective aperture radius...8.9nm^{-1}

.maximal spatial frequency for the multislice beams..............20.0nm^{-1} (625 beams)

.maximal spatial frequency for the multislice phasegrating.....40.0nm^{-1} (2500 coeffs)

.thickness of the elementary slice...0.2885nm ($|c|$)

.crystallographic data...*as in table 1****

---

*   in agreement with actual values determined (Hetherington et al., 1989). Under such conditions, the "point resolution" of the microscope appears to be limited to ≈ 0.16nm, due to the chromatic error and residual vibration (the "Scherzer resolution limit" would be around 0.14nm)

**   experimentally measured on diffraction patterns

*** readjustment of occupancy factors - according to the relations given in Table 1 - has been done for the K-mullite, for which x (0.30) slightly differs from the ideal value (0.25).

FIGURE   CAPTIONS

Figure 1: [001] projections of the structure of mullite.

a): average unit cell. Heavily outlined sites have partial occupancies and represent displaced atoms due to the presence of oxygen vacancies (see figure 1c). Dark and shaded atoms are those located at z=0.

b): perfect structure of mullite, i.e. in the hypothetical case where there is no oxygen vacancy.

c): model of atomic displacements around a vacancy on a O_3 site (displacements - indicated by arrows - allow the atoms of interest to be almost correctly re-coordinated).

Figure 2: WPO images of mullite with increasing resolution (to be compared with the inset perfect cell). Note that a resolution of at least 0.19nm is required to detect the presence of the anions, and 0.12nm is required to resolve them completely.

Figure 3: CTF for the ARM at 800 kV.

a): Scherzer defocus Δf_1 = -55nm.

b): Δf_2 = -80nm.

At Δf_2 maximum transfer is obtained in the 0.20nm to 0.17nm range since the CTF (solid line) lies hard against the chromatic aberration damping curve (dashed line). At Δf_1 some potential transfer is lost because the CTF does not lie along the damping curve.

Figure 4: experimental Scherzer micrograph of T-mullite; the inset simulated image corresponds to t = 2.3nm and Δf = -50nm (note the correspondence with the 0.19nm WPO image in figure 2). The diffraction pattern shows the incident beam convergence under imaging conditions. The diffractogram shows the spatial frequencies contributing to the image, in particular the strong 0.19nm contribution from the 400-000 interference. The inset CTF shows that frequencies much beyond 0.19nm are severely damped.

Figure 5: images of T-mullite at a defocus near Δf_2 (the experimental defocus value estimated from the diffractogram is -85nm). The image on the

bottom has been digitized and processed in order to improve the image quality. Inset calculated images correspond to t = 3nm and Δf = -85nm; the identification of the aluminium columns is somewhat tedious, due to the effect of the CTF illustrated by figure 3.

Figure 6: a): matrix of calculated images for a reasonably low thickness and different defoci (from left to right and top to bottom: Δf = +70nm, +45nm, +30nm, +10nm, 0nm, -20nm, -40nm, -60nm, -90nm, -100nm, -110nm and -140nm). b): experimental through-focus series from the T-mullite corresponding to figure 6a.

Figure 7: influence of specimen thickness on images of mullite at Scherzer defocus (T-mullite). The contrast obtained at t_3 $\approx$ 16nm is slightly modified by crystal tilt (the calculated image corresponds to a 1.9mrad tilt in the [110] direction; however, the match is not perfect, due to the extreme difficulty of determining the actual misorientation with a sufficient accuracy, even through optical or numerical diffractogram analysis).

Figure 8: effect of beam tilt (right) on the Scherzer image (left) of a 3nm thick T-mullite crystal ($\approx$ 2.7 mrad, corresponding to the beam aligned on (200); see inset diffraction pattern).

Figure 9: effect of astigmatism on HR micrographs of T-mullite. a): acceptable astigmatism correction, as revealed by the inset diffractogram (obtained from a close area where a contamination layer is present, contrary to the shown region, which exhibits a very clean edge); t and Δf are 3nm and -80nm respectively for the calculated image. b): incorrect astigmatism setting.

Figure 10: HREM analysis of a thin uniform crystal edge in K-mullite.
a): low magnification micrograph taken at Scherzer defocus (-50nm); details A and B are examined in figure 10b and d respectively; arrows indicate similar defects as the one studied in figure 10d.
b): through-focus series from detail A in figure 10a (from left to right: Δf = -50nm, -87.5nm, -97.5nm, -117.5nm; the thickness used in the superimposed

calculated images is 1.4nm, but identical contrasts are obtained within ± 0.5nm).

c): corresponding calculated images for a hypothetical structure where oxygen atoms are missing (without any atomic displacements); note the disagreement with experimental images from figure 10b.

d): enlargement of detail B for three defoci (-50nm, -87.5nm and -97.5nm); arrows in the first micrograph indicate a distortion of triplets of dark dots (see details in appendix)

e): calculated images matching the previous experimental micrographs; these correspond to a 0.9nm thin crystal with two vacancies along the central O_3-type oxygen column, according to the model of figure 1c (see appendix).

Figure A1: matrix of calculated images of a defect crystal containing various numbers of oxygen vacancies along an O_3-type column, according to the model of figure 1c (see text). The three images in each group correspond to the defocus values determined for the experimental images of figure 10d.

Figure A2: drawings showing the three features allowing consistent analysis of figures 10d-e and A1 (see text).

Figure A3: hypothetical contrast produced by the presence of a vacant O_3-type column (arrow) without atomic displacement: no defect can be detected (t = 1.4nm, Δf = - 50nm, -87.5nm and -97.5nm respectively).

Figure A4: probability p(0.5,t) as a function of thickness in the case of the K-mullite (see text). The curve corresponding to a random distribution of vacancies is shown in full line, and the results obtained with the restriction "no nearest-neighbour vacancies" constitute the dashed line.

Fig. 1

XBL 893-948

0.38 nm 0.34 0.24

0.19 0.17 0.12

XBB 893-2029

Fig. 2

SHRLI82A - FIRST-ORDER PHASE CONTRAST TRANSFER FUNCTION(S)
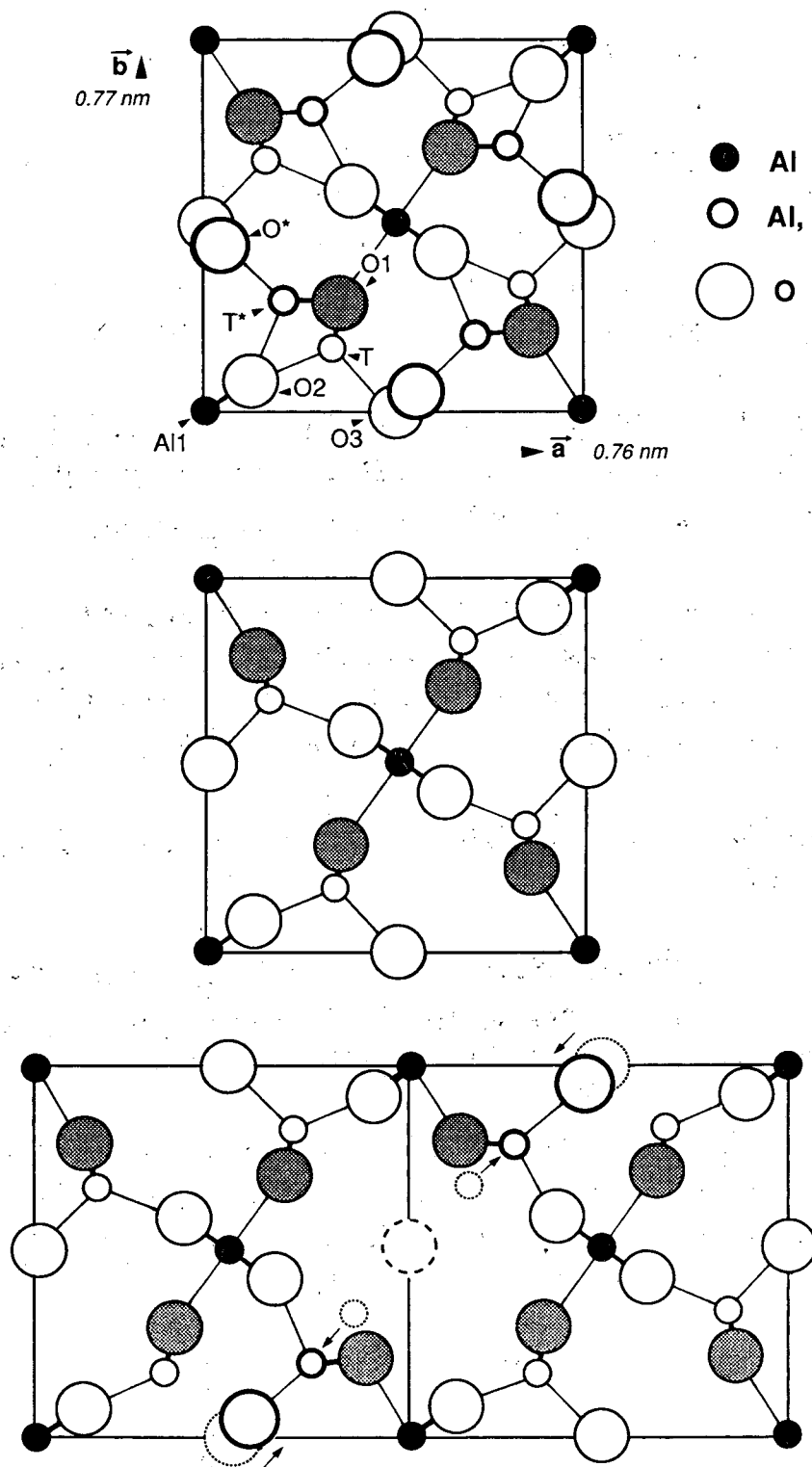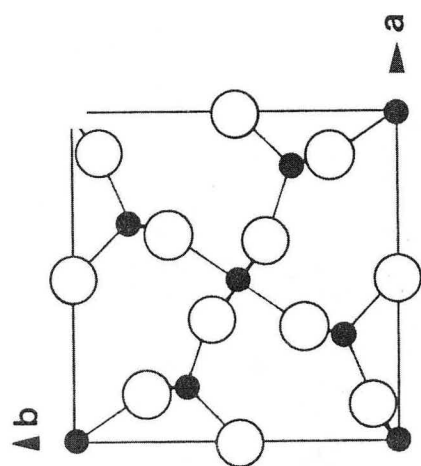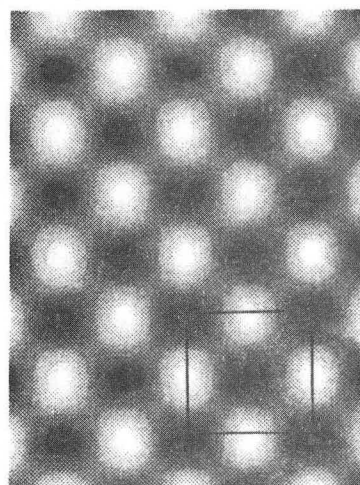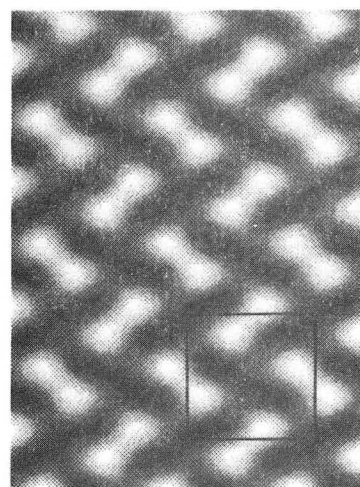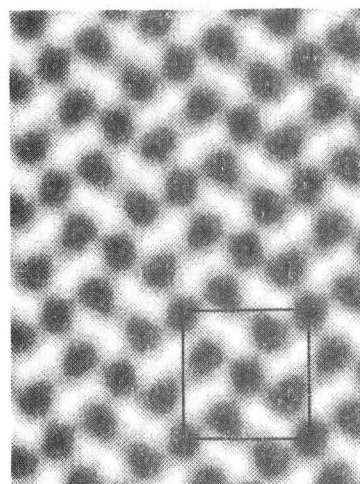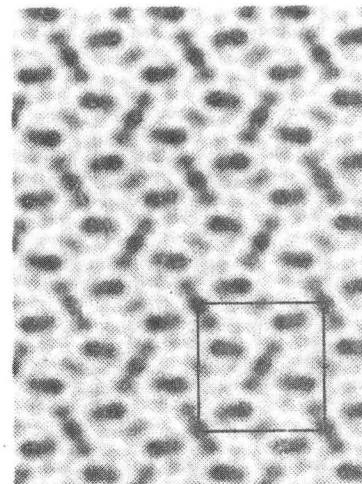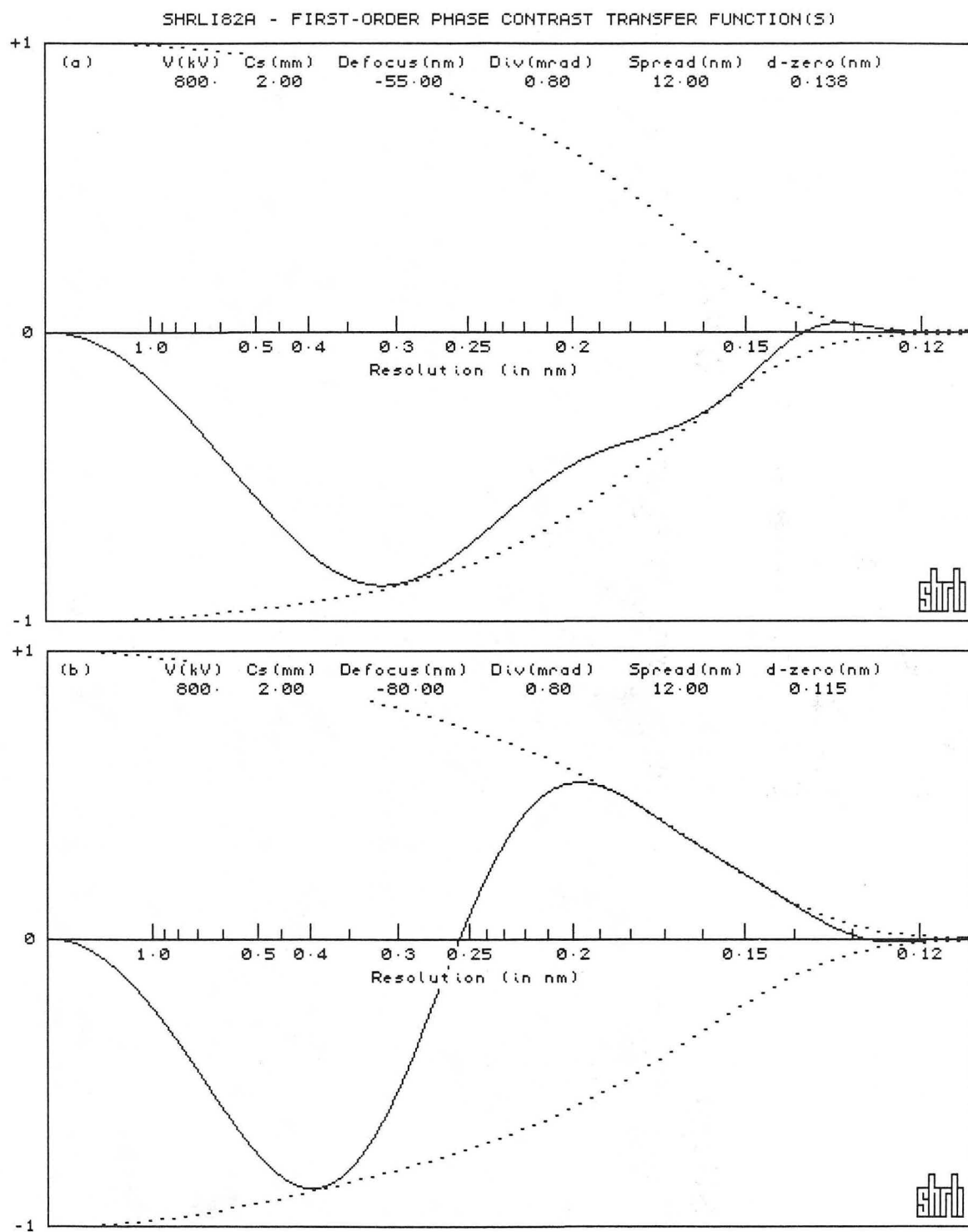
XBL 895-1864

Fig. 3

XBB894-3208

Fig. 4

0.76 nm

− 85 nm

Al₁
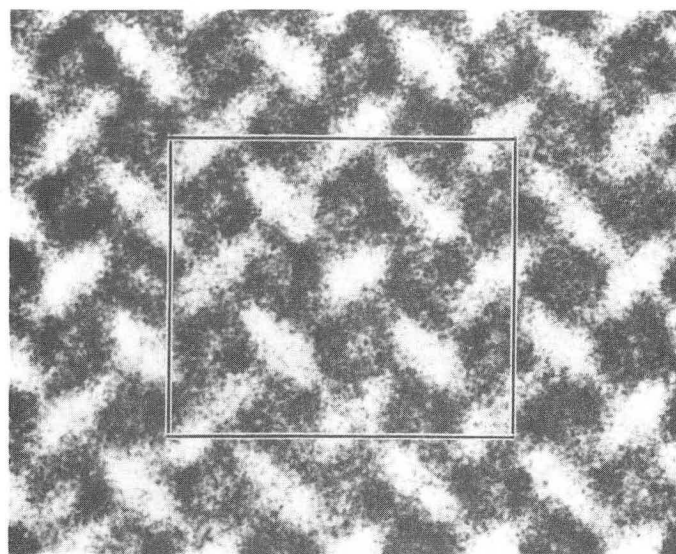
Fig. 5

Fig. 6

t = 4.5 nm
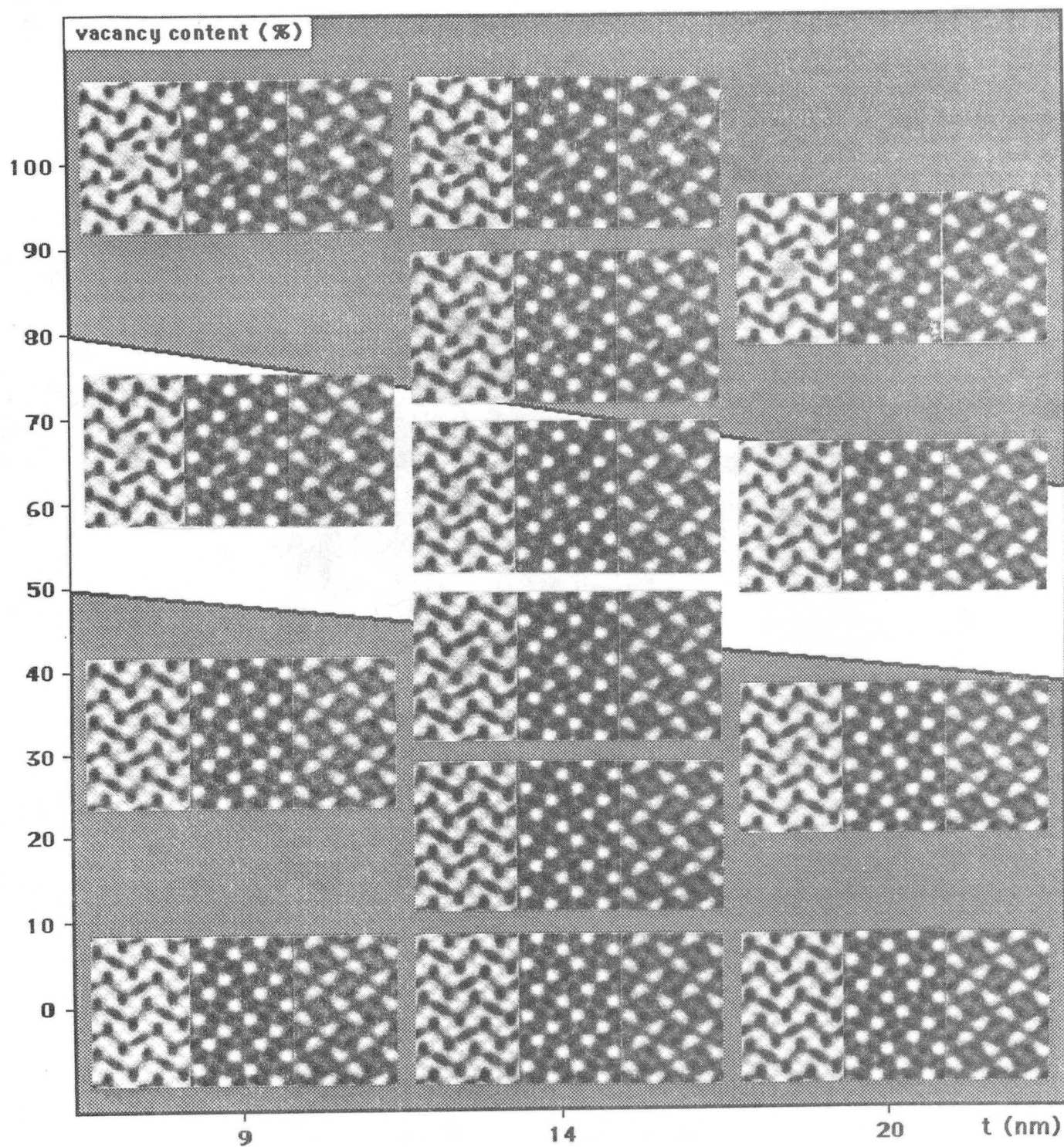
Fig. 7

0.76 nm

.200
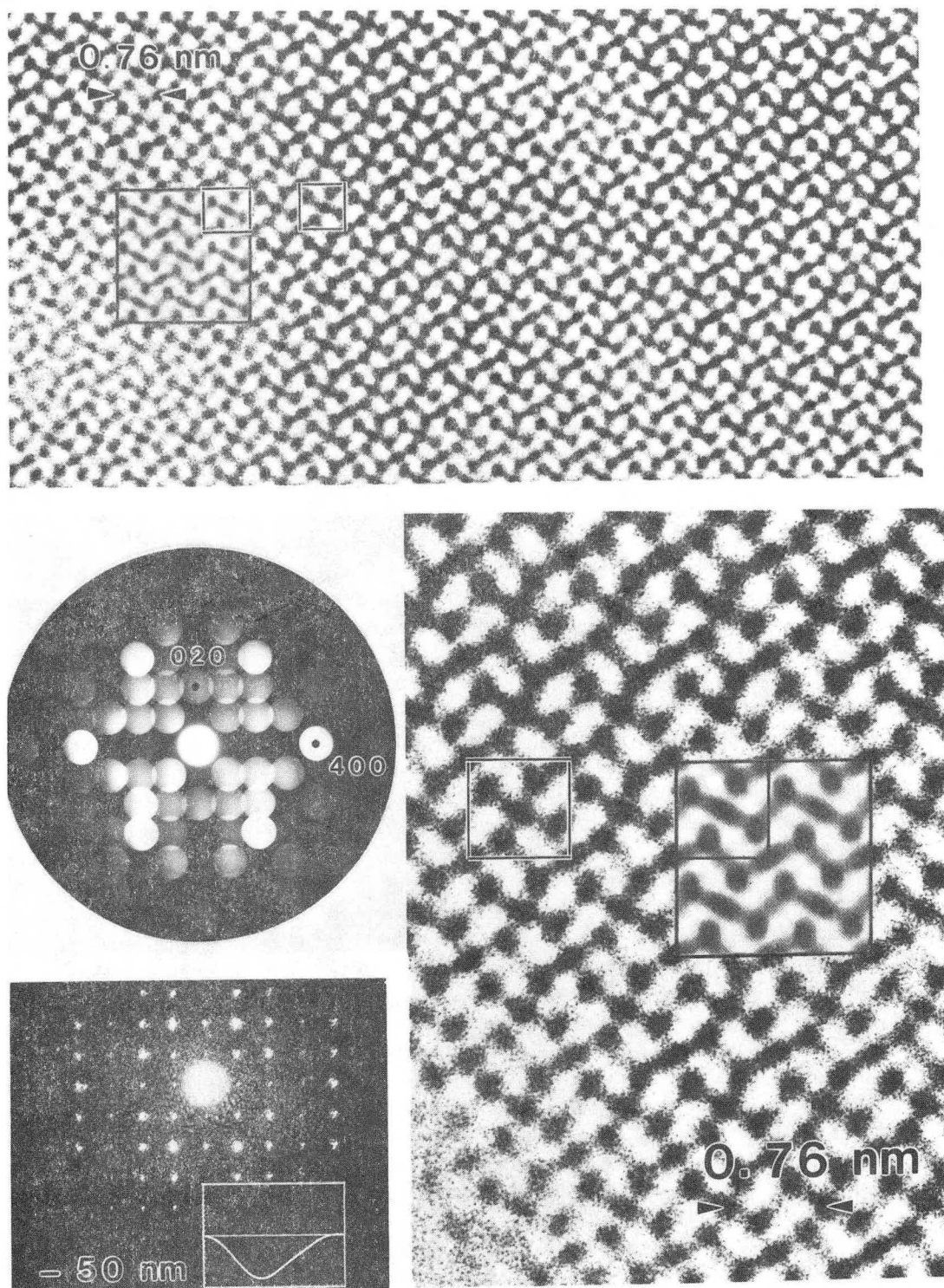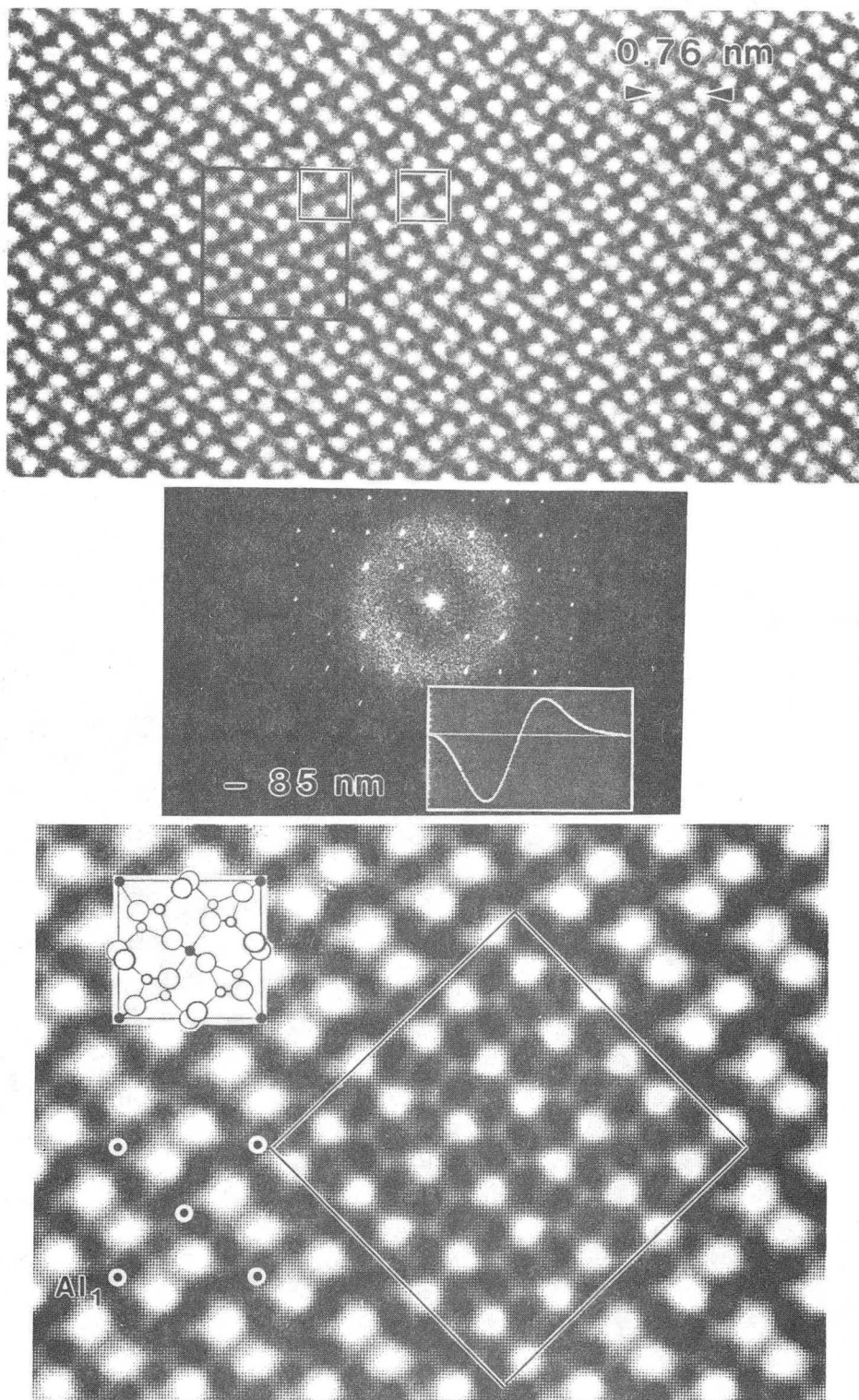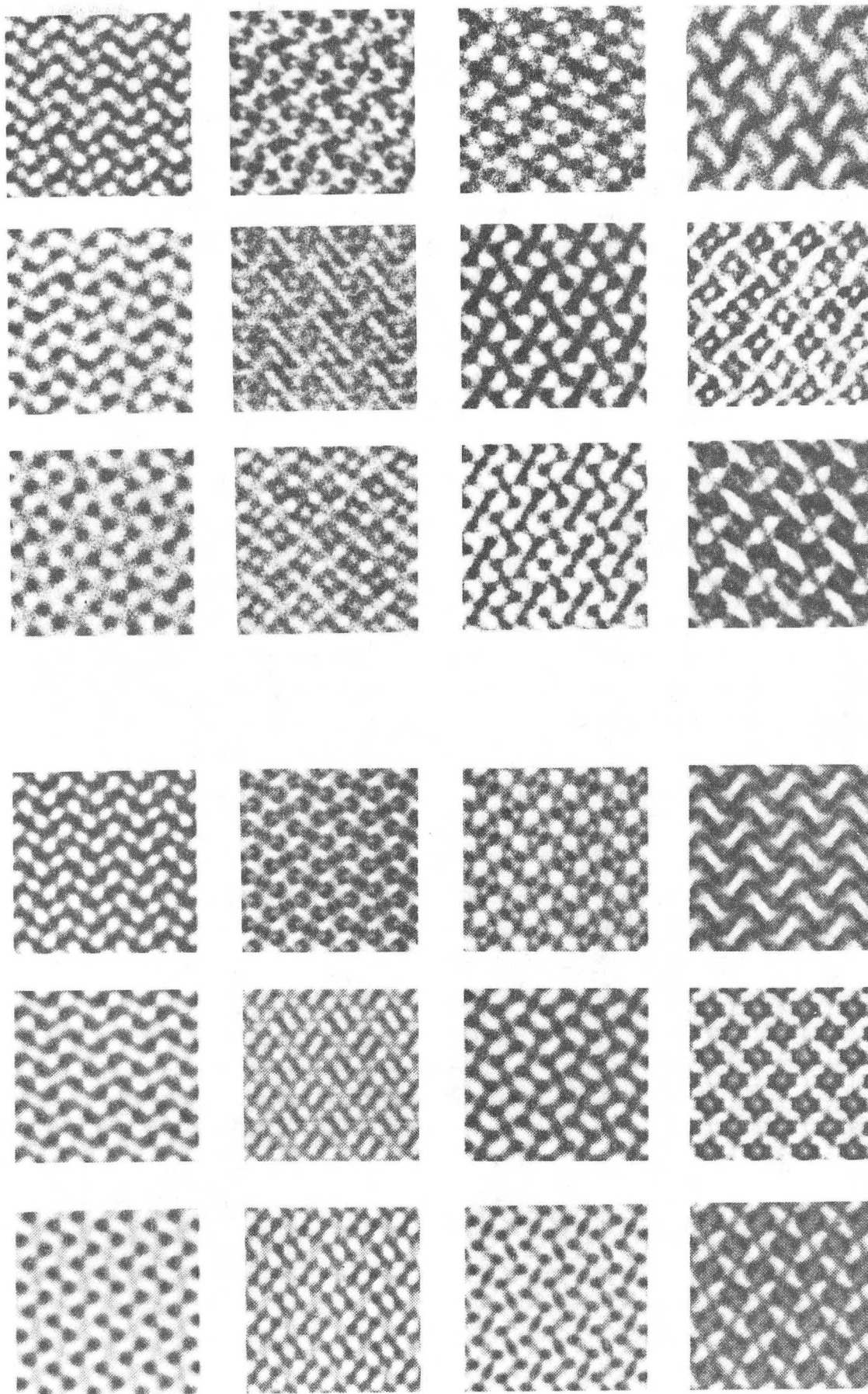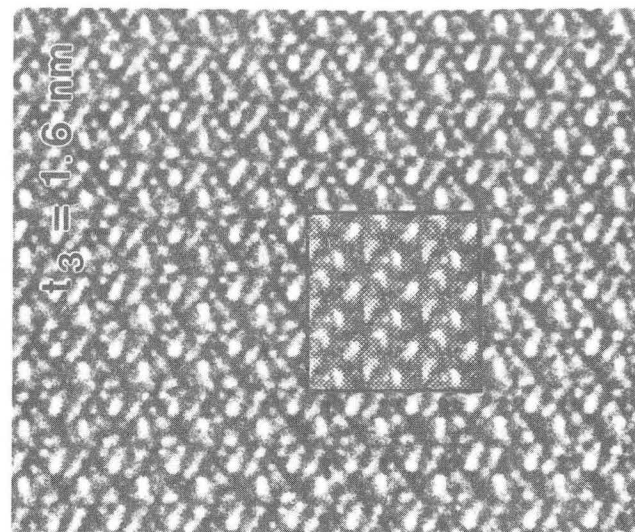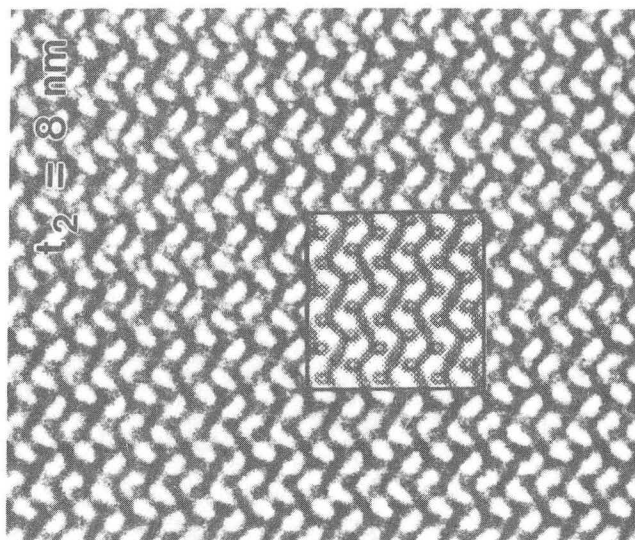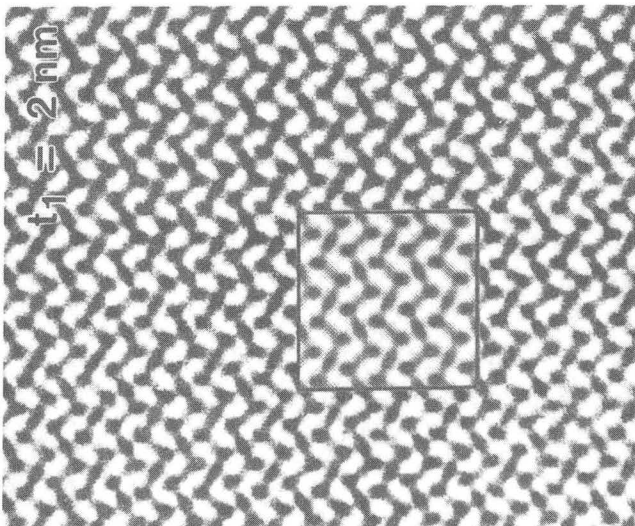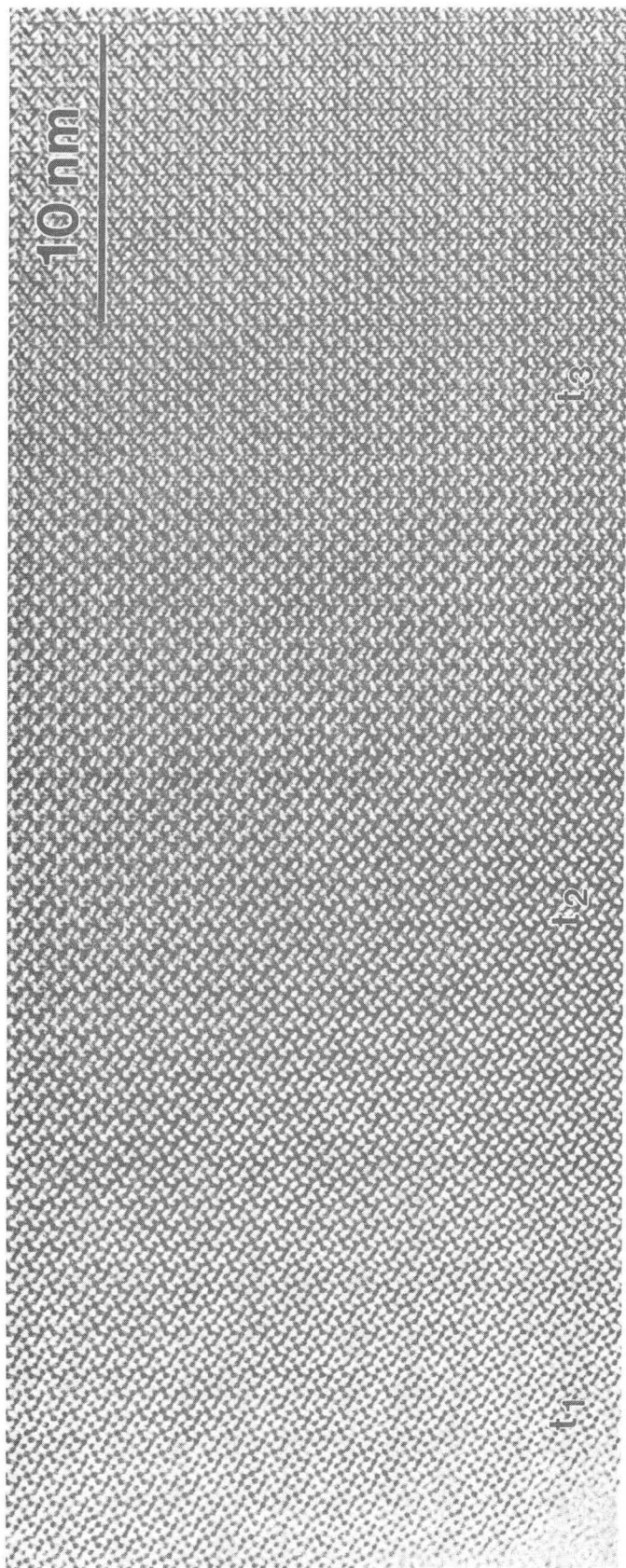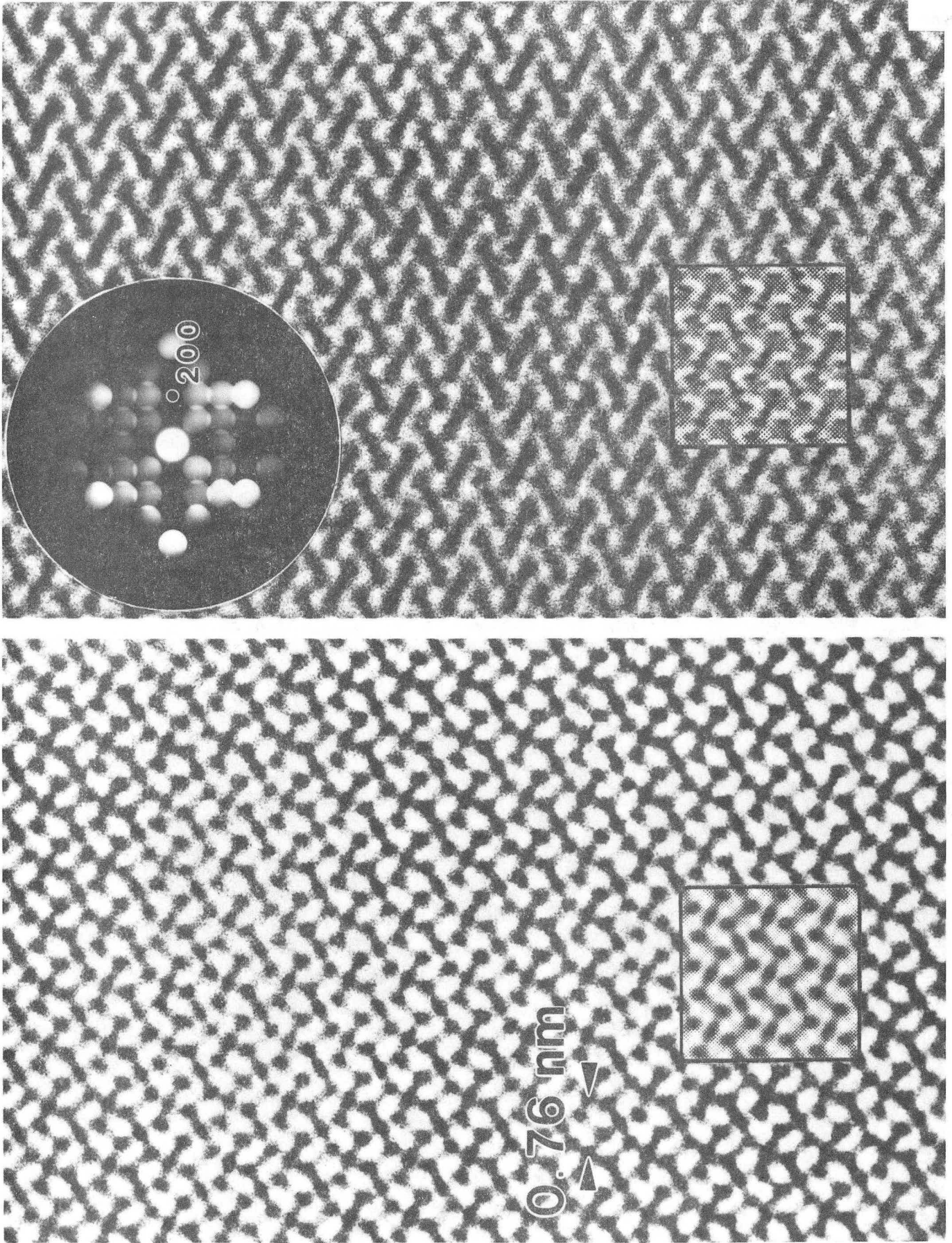
Fig. 8

XBB 893-2207

Fig. 9

Fig. 10a,b,c

0.76 nm
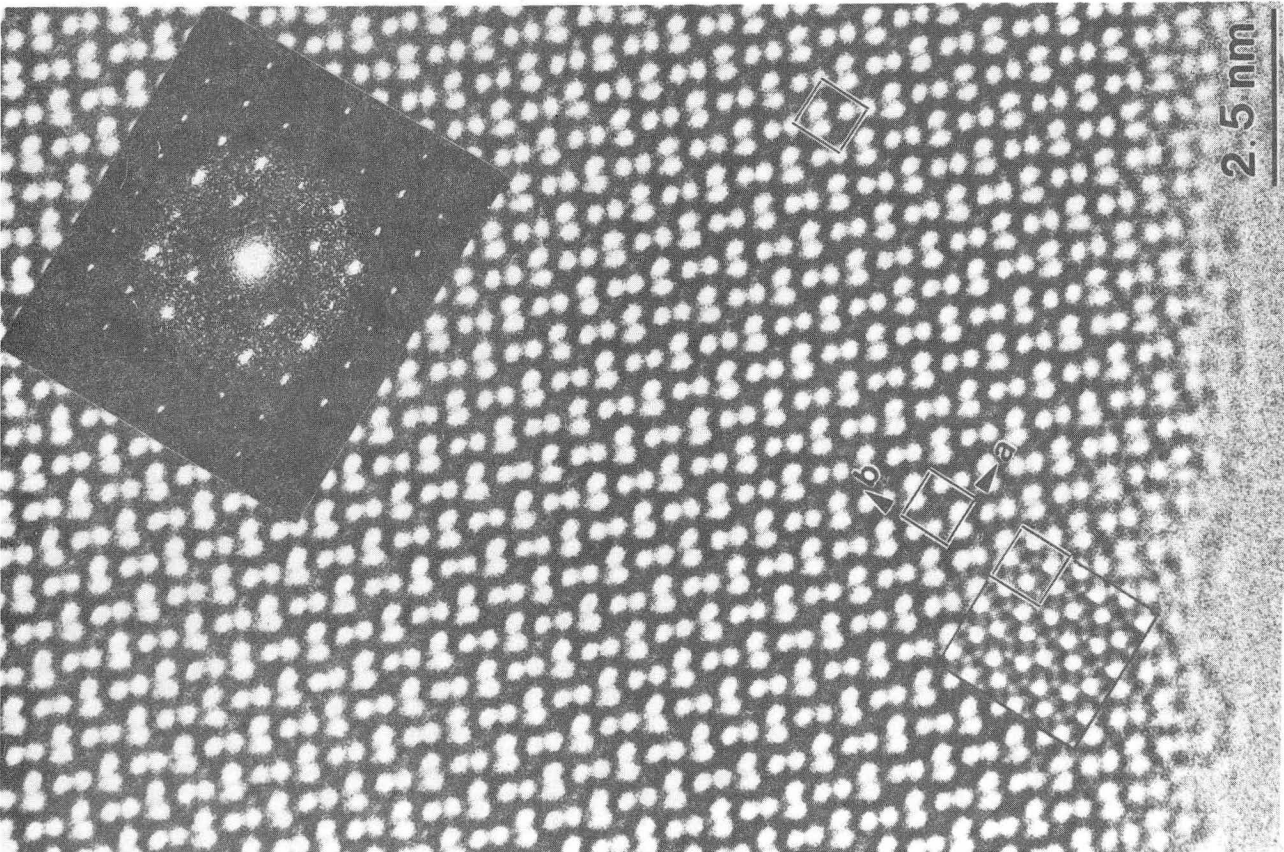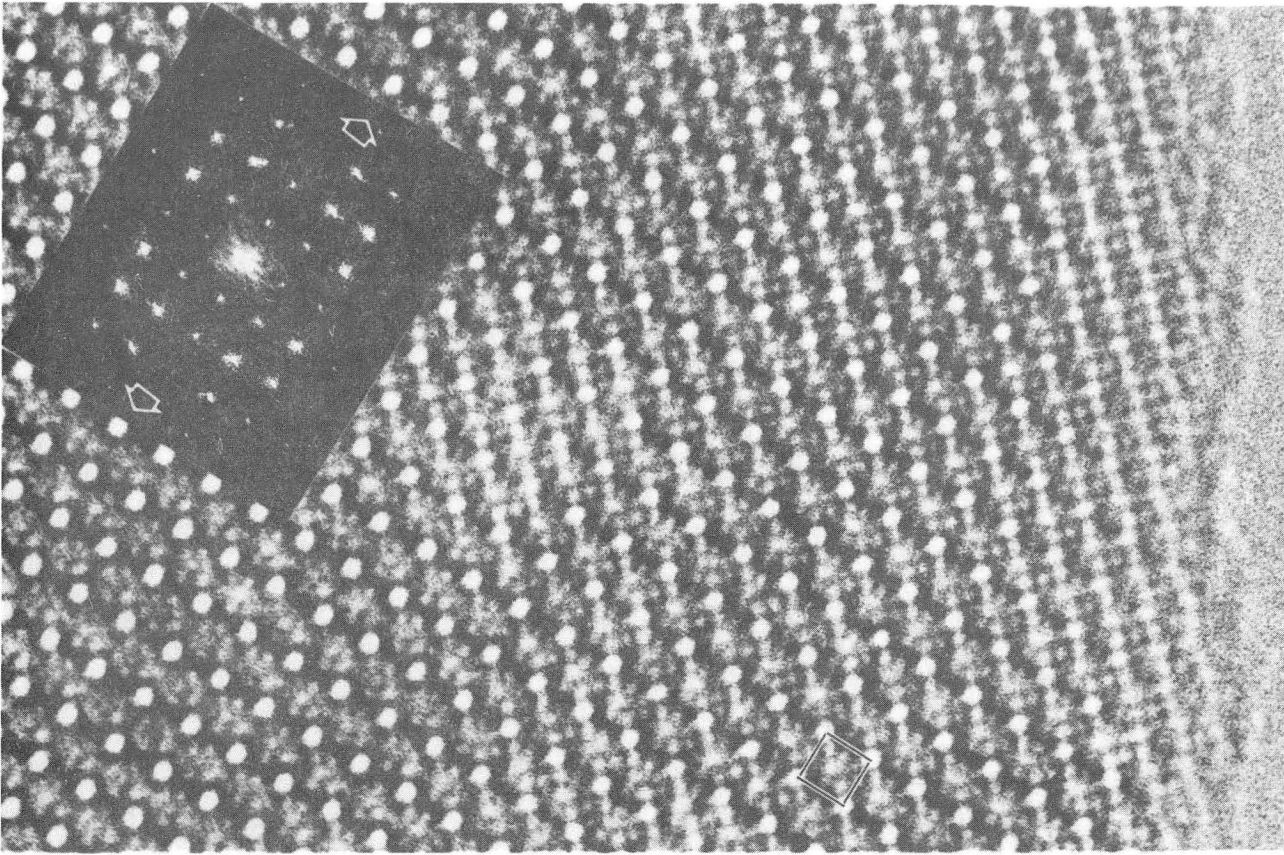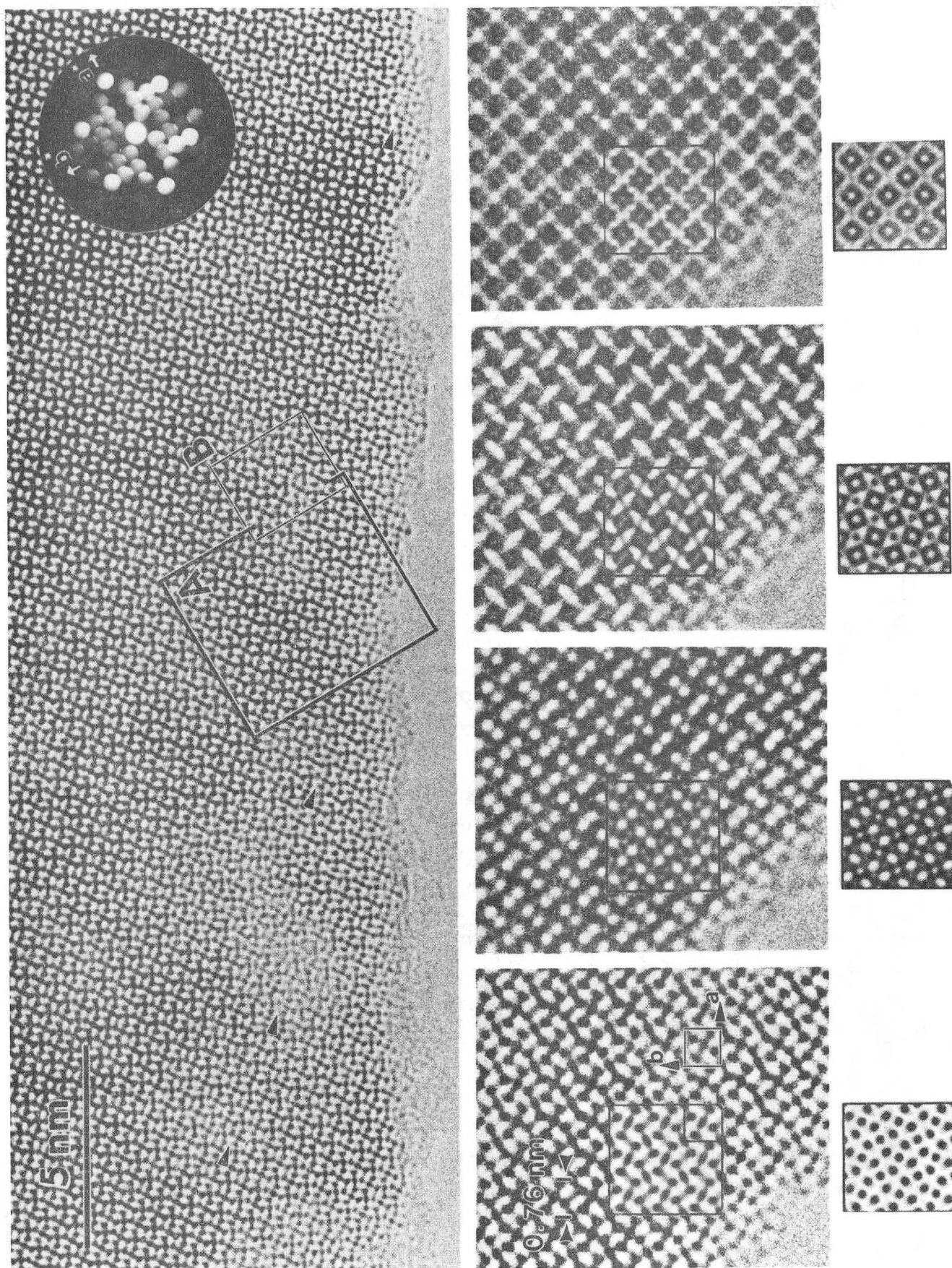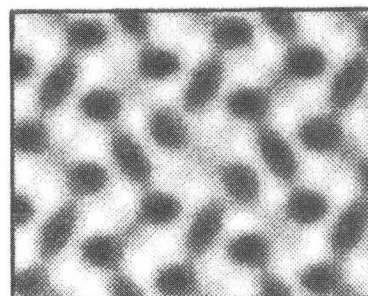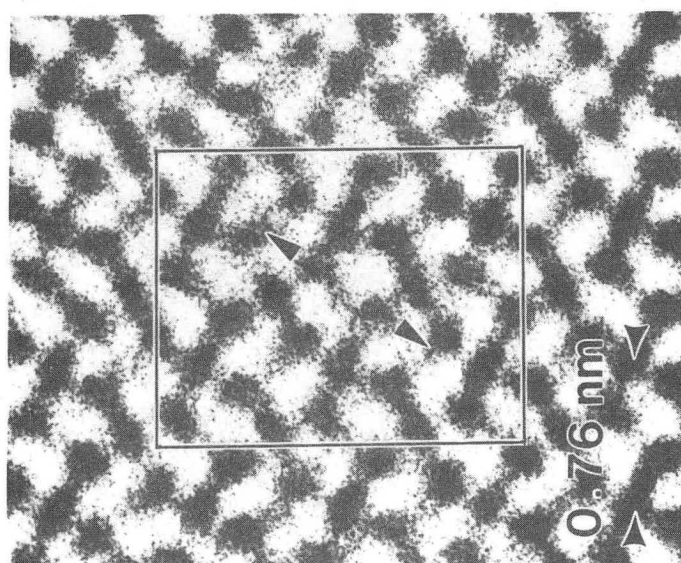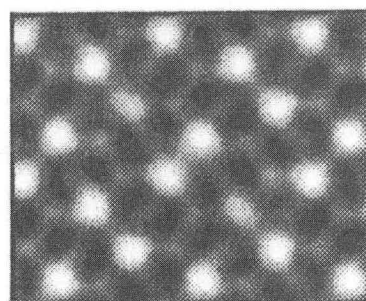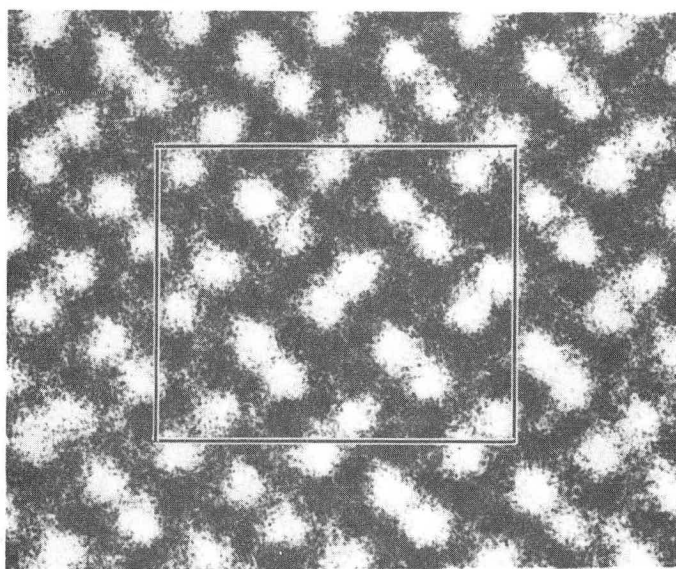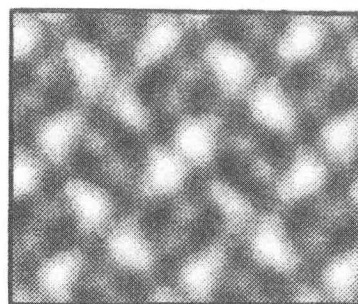
Fig. 10d,e

XBB 894-3209

Fig. A1
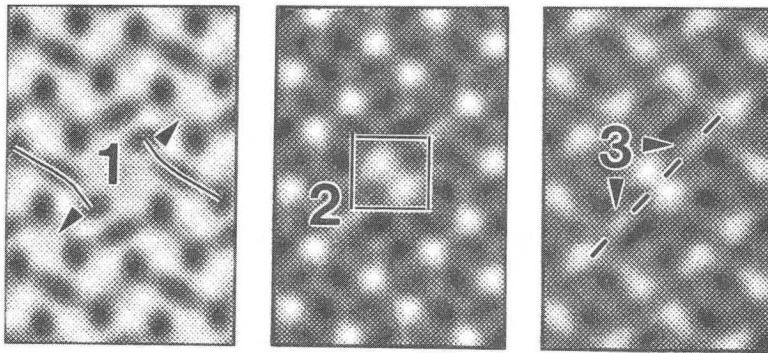
XBB 894-3211

Fig. A2

XBB 894-3212

Fig. A3

XBL 894-1470

Fig. A4